Moiré Lattice in One-Dimensional Synthetic Frequency Dimension

Danying Yu,[1] Guangzhen Li,[1] Luojia Wang,[1] Daniel Leykam,[2,*] Luqi Yuan,[1,†] and Xianfeng Chen[1,3,4]
[1]State Key Laboratory of Advanced Optical Communication Systems and Networks, School of Physics and Astronomy, Shanghai Jiao Tong University, Shanghai, 200240, China
[2]Centre for Quantum Technologies, National University of Singapore, 3 Science Drive 2, 117543, Singapore
[3]Shanghai Research Center for Quantum Sciences, Shanghai, 201315, China
[4]Collaborative Innovation Center of Light Manipulations and Applications, Shandong Normal University, Jinan, 250358, China

(Received 31 August 2022; accepted 13 March 2023; published 7 April 2023)

The moiré lattice has recently attracted broad interest in both solid-state physics and photonics where exotic phenomena in manipulating the quantum states are explored. In this work, we study the one-dimensional (1D) analogs of "moiré" lattices in a synthetic frequency dimension constructed by coupling two resonantly modulated ring resonators with different lengths. Unique features associated with the flatband manipulation as well as the flexible control of localization position inside each unit cell in the frequency dimension have been found, which can be controlled via the choice of flatband. Our work therefore provides insight into simulating moiré physics in 1D synthetic frequency space, which holds important promise for potential applications toward optical information processing.

DOI: 10.1103/PhysRevLett.130.143801

Moiré lattices constructed by two periodic layers stacked with a relative angle attract great interest in the solid-state physics, exhibiting exotic phenomena [1–10] including strong electron correlation [4], topological mosaics [5], moiré excitons [9], and fractional Chern insulators [10]. Recently, photonic analogs of moiré lattices taking advantage of simple photonic geometries to manipulate light attract to attention [11–16], demonstrating rich physics such as optical solitons [12], localization and delocalization of light [13], and on-chip light trapping [16]. Various simulation methods utilizing coupled-mode theory [14] and applying high-dimensional plane wave expansion [15] have been developed. Recently, one-dimensional (1D) analogs of moiré lattices [17] having the capability of exploring physics associated with the moiré lattice in simpler geometry trigger interest. For example, gauge fields in photonic metacrystals [18], almost-perfect flatbands, and unconventional localization in photonic crystals [19], and widely tunable Q factors in integrated silicon photonic nanowires [20] have been successively explored in one spatial dimension. On the other hand, constructing photonic lattices with synthetic dimensions attracts growing attention for simulating physics with simple structures [21–23], which therefore raises a natural question: can a 1D photonic moiré lattice be explored with few coupled rings [24–27]?

Here, we study a 1D analog of a "moiré" lattice along the frequency axis of light in two coupled ring resonators with different lengths under modulations. Two sublattices are constructed by applying resonant modulations on both rings [28], with their relative sizes playing the role of the twist angle between two sublattices. Together with the coupling between two rings, our proposed model constructs a synthetic 1D moiré lattice in the frequency dimension. We apply the transfer-matrix method [29], which crucially takes into account off-resonant modes of the coupled ring system. The nonflat to flat band transition in the synthetic space can be realized by engineering the coupling strength between two rings. We find that each spectral flatband corresponds to one localized mode with controllable localization position in one spectral unit cell. In contrast to peculiar nearly flat topological bands in two-dimensional moiré lattice at a magic angle wherein the localization position is fixed in the momentum space [30], the localization frequency inside one unit cell can be selectively excited. Furthermore, different from previous work of exploring the flatband in synthetic two-dimensional Lieb lattice [31], our study shows that there exists a correspondence between the flatband and the detailed localization position in each spectral unit cell, which thus provides a new direction towards controlling frequency conversions and localized frequency modes based on the moiré physics. Our work also holds important promise for potential applications towards the optical channel selection [32] and optical signal coding [33] with experimental reconfigurability and flexibility in synthetic frequency dimension.

We consider two rings with different lengths [see Fig. 1(a)]. The circumference of ring A (B) is $L_A = L/N_A$ ($L_B = L/N_B$). L is a length constant and $N_A(N_B)$ is a positive integer. The free spectral range (FSR) of ring A (B) is $\Omega_A = 2\pi v_g/L_A$ ($\Omega_B = 2\pi v_g/L_B$), with v_g being

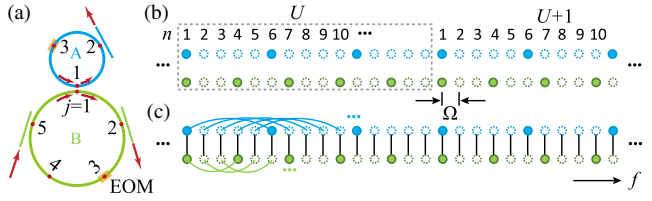

FIG. 1. (a) Schematic of two coupled rings with relative lengths $\Omega_A:\Omega_B = 5:3$, each of which are divided into equal-length parts. (b) All possible modes of ring A (B) in blue (green) circles are separated by Ω, where resonant (nonresonant) ones are labeled by solid (hollow) circles. The dashed rectangle denotes one unit cell. (c) All modes are coupled through resonant modulations in both rings (blue and green lines). Black lines represent couplings between modes in ring A and ring B at the same frequency.

the group velocity. Resonant frequencies in ring A (B) are $\omega_{A,m} = \omega_0 + m\Omega_A = \omega_0 + mN_A\Omega$ ($\omega_{B,m} = \omega_0 + m\Omega_B = \omega_0 + mN_B\Omega$), where ω_0 is the reference frequency which is set to be equal for ring A and ring B, m is an integer, and $\Omega = 2\pi v_g/L$, shown in Fig. 1(b). Each unit cell in frequency dimension has the range of $N_AN_B\Omega$. U labels the index of a unit cell and n denotes all possible mode in one unit cell. Two nearest sites are separated by Ω in frequency dimension. We perform electro-optic modulation (EOM) inside ring A (B) resonantly at Ω_A (Ω_B) with modulation strength $\alpha(\beta)$. In each ring, a synthetic lattice in frequency dimension is therefore created. Note when Ω_A/Ω_B is an irrational number the formed lattice is quasiperiodic [34–38]. However, here we consider cases where Ω_A/Ω_B are rational numbers, so there exists a large unit cell in frequency dimension, associated to a 1D bichromatic moiré lattice [17].

Two rings are coupled. Because of the different lengths of two rings, the optical field at a resonant mode in one ring leaks energy into another ring, where the field becomes nonresonant [see Fig. 1(c)]. We find that the roles of these possible nonresonant modes cannot be simply ignored, because EOMs convert the frequencies of these modes and then energies of these converted nonresonant modes may couple into the other rings, before the energy of the nonresonant mode dissipates. The model here constructs a one-dimensional synthetic moiré lattice in frequency dimension. Such a synthetic lattice contains characteristics of 1D analogs of moiré lattice, where the ratio of relative sizes of two sublattices along the frequency dimension is given by two coprime integers, such as 5:3, as an analog of twist angle in two-dimensional lattice. Even though 1D analogs of moiré lattices have been studied in cold atom systems [17] and photonic crystals [19,20], our model is fundamentally different, not only in a sense of using a synthetic lattice in frequency dimension, but also due to the fact that the minor effect from nonresonant modes is included, enabling a scheme to manipulate the localization position inside one unit cell.

To explore our model, we introduce the transfer-matrix method [29], which is briefly summarized here. We consider all possible modes labeled as $\omega_{U,n} = \omega_0 + (U-1)N_AN_B\Omega + n\Omega$, where $U = 1, 2, \ldots$ and $n = 1, 2, \ldots, N_AN_B$. As an example, we show the physical geometry of rings and 1D synthetic moiré lattice with ratio $\Omega_A:\Omega_B = N_A:N_B = 5:3$ in Fig. 1. To apply the transfer-matrix method, we divide each ring into equal length segments, so light undergoes a sequence of alternating free propagation for a fixed time $\delta t = L/(N_AN_Bv_g)$ followed by scattering involving a change in its frequency via modulation, coupling into the other ring, or coupling to the external waveguides used for input or output, as illustrated in Fig. 1(a) [39]. We label scattering points as $j = 1, \ldots, N_B(N_A)$. The optical field at each scattering point j is expanded by modal amplitudes $a_{j,U,n}(b_{j,U,n})$ with carrier frequency $\omega_{U,n}$ in ring A (B).

We study the scattering process with discrete time variables $t_{i+1} = t_i + \delta t$. The transfer process between scatter points is given by

$$a_{j+1,U,n}(t_{i+1}) = e^{i\delta\omega\cdot\delta t}e^{i\beta_n' L/(N_AN_B)}a_{j,U,n}(t_i), \quad (1)$$

$$b_{j+1,U,n}(t_{i+1}) = e^{i\delta\omega\cdot\delta t}e^{i\beta_n' L/(N_AN_B)}b_{j,U,n}(t_i), \quad (2)$$

where $\delta\omega$ is frequency detuning and $\beta_n' = \omega_{U,n}/v_g$ is wave vector satisfying $e^{i\beta_n' L/(N_AN_B)} = e^{i2(n-1)\pi/(N_AN_B)}$. We perform EOMs at $j = 3$ in both rings, modulated by synchronized signals at $\alpha\cos(\Omega_A t)$ and $\beta\cos(\Omega_B t)$, which provides [42]

$$a_{3,U,n}(t_i^+) = \sum_{U',n'} a_{3,U',n'}(t_i^-) i^{q_{N_A,U',n'}} J_{q_{N_A,U',n'}}(\alpha), \quad (3)$$

$$b_{3,U,n}(t_i^+) = \sum_{U',n'} b_{3,U',n'}(t_i^-) i^{q_{N_B,U',n'}} J_{q_{N_B,U',n'}}(\beta), \quad (4)$$

where $q_{N_A,U',n'} = [N_AN_B(U'-U) + n' - n]/N_A$, $q_{N_B,U',n'} = [N_AN_B(U'-U) + n' - n]/N_B$ are integers corresponding to the spacing between two modes. $J_{q_{N_A,U',n'}}(\alpha)$ [$J_{q_{N_B,U',n'}}(\beta)$] is the Bessel function of the first kind and $t_i^{\pm} = t_i + 0^{\pm}$. The coupling between two rings at $j = 1$ gives [43]

$$\begin{pmatrix} a_{1,U,n}(t_i^+) \\ b_{1,U,n}(t_i^+) \end{pmatrix} = \begin{pmatrix} \sqrt{1-\gamma^2} & -i\gamma \\ -i\gamma & \sqrt{1-\gamma^2} \end{pmatrix} \begin{pmatrix} a_{1,U,n}(t_i^-) \\ b_{1,U,n}(t_i^-) \end{pmatrix}, \quad (5)$$

where γ is the coupling strength between two rings.

Thus, we obtain a complete set of Eqs. (1)–(5) that describes the propagation and conversion of light circulating in two rings. By substituting Eqs. (3)–(5) into Eqs. (1) and (2), we can re-write the dynamic process into an evolution function

$$\psi(t_{i+1}) = e^{i\delta\omega\cdot\delta t}H\psi(t_i), \quad (6)$$

where H is the matrix form of the transfer relationship between each optical component and $\psi(t_i) = \Big[\ldots, \underbrace{\underbrace{a_{1,U,1}(t_i), \ldots, a_{N_B,U,1}(t_i), b_{1,U,1}(t_i), \ldots, b_{N_A,U,1}(t_i)}_{n=1}, \underbrace{\ldots, a_{j,U,2}(t_i), \ldots, b_{j,U,2}(t_i), \ldots}_{n=2}, \ldots}_{U}, \underbrace{\underbrace{a_{1,U+1,1}(t_i), .., b_{j,U+1,1}(t_i), \ldots}_{n=1}, \ldots}_{U+1}, \ldots, \ldots\Big]^T$. The corresponding band structure in the k_f space can then be obtained. We consider the lattice is infinite, so the translation symmetry holds with spectral periodicity $N_A N_B \Omega$. Fourier transforms $a_{1,k_f,n} = \sum_U a_{1,U,n} e^{-ik_f U N_A N_B \Omega}$ ($b_{1,k_f,n} = \sum_U b_{1,U,n} e^{-ik_f U N_A N_B \Omega}$) are applied and Eq. (6) becomes $\psi_{k_f} = e^{i\delta\omega\cdot\delta t} H_{k_f} \psi_{k_f}$, where H_{k_f} is the transfer-matrix form in the k_f space and $\psi_{k_f} = \Big[\underbrace{a_{1,k_f,1}, \ldots, a_{N_B,k_f,1}, b_{1,k_f,1}, \ldots, b_{N_A,k_f,1}}_{n=1}, \underbrace{\ldots, a_{j,k_f,2}, \ldots, b_{j,k_f,2}, \ldots}_{n=2}, \ldots\Big]^T$. In the steady-state limit, we obtain the eigenfunction equation as $e^{-i\delta\omega\cdot\delta t}\psi_{k_f} = H_{k_f}\psi_{k_f}$. The band structure between frequency detuning ($\delta\omega$) and reciprocal lattice vector (k_f) is therefore obtained by diagonalizing H_{k_f} and taking the natural logarithm of eigenvalues [29]. Since $\delta\omega\delta t$ is a phase factor, $\delta\omega \in [-N_A N_B \Omega/2, N_A N_B \Omega/2]$.

We here analyze band structures of three 1D synthetic moiré lattices with different ratios of $\Omega_A : \Omega_B = N_A : N_B = 4:3, 5:3$, and $7:5$, respectively, while choosing $\alpha = 0.2$, $\beta = 0.2$, and varying γ. We define P to quantify the eigenstate distribution ratio between ring A and ring B:

$$P = \left[\frac{\sum_{n=1}^{N_A N_B}\sum_{j=1}^{N_B}|a_{j,k_f,n}|^2}{N_B} - \frac{\sum_{n=1}^{N_A N_B}\sum_{j=1}^{N_A}|b_{j,k_f,n}|^2}{N_A}\right] \Big/ \left[\frac{\sum_{n=1}^{N_A N_B}\sum_{j=1}^{N_B}|a_{j,k_f,n}|^2}{N_B} + \frac{\sum_{n=1}^{N_A N_B}\sum_{j=1}^{N_A}|b_{j,k_f,n}|^2}{N_A}\right], \quad (7)$$

where $P = 1(-1)$ denotes that the energy of the eigenstate is fully distributed on modes in ring A (B). We plot $\delta\omega$ with the labeled P in the k_f dimension for $\gamma = 0.1$ in Figs. 2(a)–2(c). The band structures hold the periodicity of Ω and the regime of $\delta\omega \in [-\Omega/2, \Omega/2]$ is of practical importance, which results in 7, 8, 12 bands inside this regime in three lattice structures, respectively. The number of bands in $\delta\omega \in [-\Omega/2, \Omega/2]$ is consistent with the number of resonant modes in one unit cell. As the example of $\Omega_A : \Omega_B = 5:3$ where 8 resonant modes are in one unit cell [see Fig. 1(b)], there are 8 bands in Fig. 2(b). One can see that, in Figs. 2(a)–2(c), all bands are nonflat, while eigenstate distribution ratios, P, change for different k_f. Projected band structures versus γ are shown in Figs. 2(g)–2(i), where increasing γ leads each band to eventually become flat. There exists threshold γ_s, as indicated by the red dashed line for each lattice structure ($\Omega_A : \Omega_B = 4:3, 5:3, 7:5$). For γ larger than γ_s, the band structure exhibits the flat feature and uniform eigenstate distribution, where the criterion of γ_s can been found in the Supplemental Material [39]. In Figs. 2(d)–2(f), we plot band structures at $\gamma = \gamma_s$ for three lattice structures. All bands are flat, and also P remains unchanged when varying k_f. We find that, once $\gamma \geq \gamma_s$, the bands are highly flat, with very small fluctuations $\lesssim 1\%$ of the maximum bandwidth. In general, γ plays a key role in controlling the nonflat to flat band transition. One sees that γ_s for the lattice structure with $\Omega_A : \Omega_B = 7:5$ is the smallest, while γ_s for the case of $\Omega_A : \Omega_B = 4:3$ is the largest in three structures. Such transition occurs between two limits, i.e., the weak coupling limit ($\gamma \lesssim 0.1$) and the strong coupling limit ($\gamma \to 1$) [39]. Especially for $\gamma = 1$, the coupled two rings effectively become one large ring and, consequently, the modulations are no longer resonant, hence perfectly flat bands are expected. Nevertheless, highly flat bands appear well before the strong coupling limit (i.e., $\gamma < 1$), as interactions between the mismatched modes in the two rings via the coupling become stronger

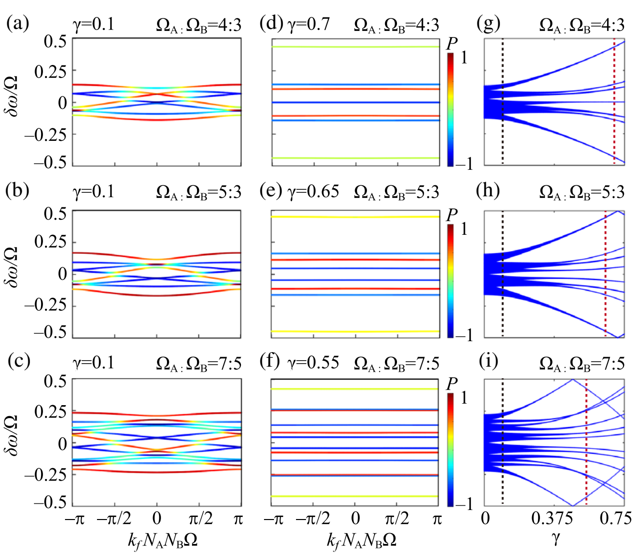

FIG. 2. The band structures of 1D synthetic moiré lattices for different ratios of $\Omega_A : \Omega_B$, (a)–(c) at $\gamma = 0.1$ and (d)–(f) at $\gamma = \gamma_s$. (g)–(i) The projected bandstructures versus γ, where black dashed lines denote $\gamma = 0.1$ and red dashed lines denote $\gamma = \gamma_s$.

when γ is increasing, and finally overcome effects of connectivities between modes in each ring via the resonant modulations. In the following, we choose the case of $\Omega_A:\Omega_B = 5:3$ to further illustrate the characteristic of flatbands.

We examine the eigenstate distribution for 8 nondegenerate flatbands in the structure with $\Omega_A:\Omega_B = 5:3$ at $\gamma = \gamma_s = 0.65$. In Fig. 3, we plot the corresponding normalized eigenstate distributions of 8 bands at $k_f = -\pi/(N_A N_B \Omega)$, which are defined as

$$|a_n|^2 = \frac{1}{\mathcal{N}} \frac{1}{N_B} \sum_{j=1}^{N_B} |a_{j,k_f,n}|^2, \tag{8}$$

$$|b_n|^2 = \frac{1}{\mathcal{N}} \frac{1}{N_A} \sum_{j=1}^{N_A} |b_{j,k_f,n}|^2, \tag{9}$$

where $\mathcal{N} = \sum_n [(1/N_B) \sum_{j=1}^{N_B} |a_{j,k_f,n}|^2 + (1/N_A) \times \sum_{j=1}^{N_A} |b_{j,k_f,n}|^2]$ is the normalization coefficient. Figures 3(a)–3(h) correspond to the band index of the first band to the eighth band in Fig. 2(e) in the order from top to bottom. One can see the striking feature is that each eigenstate distribution shows the localization of the energy on nearly one site inside the unit cell along the frequency dimension, though the ratio between $|a_n|^2$ and $|b_n|^2$ is different. We show the eigenstate distributions at one k_f in Fig. 3. However, we find that the trend of eigenstate distributions remains almost the same throughout the entire k_f space, which is also inferred from Fig. 2(e). The eigenstates distribute at 7 frequencies in one unit cell, so we can denote site $n = 1,4,6,7,10,11,13$ as frequency channels 1 to 7, respectively. In Fig. 3(i), we plot the quantity $|a_n|^2 + |b_n|^2$ with the band index and frequency channel (see more description of the relationship between band index and localization position in Supplemental Material [39]). In contrast to two-dimensional moiré lattice at the magic-angle, where the peculiar nearly flat topological bands are obtained by combining a trivial flatband ("heavy fermions") and gapless topological semimetal bands, resulting in the localization position being fixed at the AA-stacking regions of one unit cell [30], we take advantage of mode couplings between two rings to obtain the selective excitation of different frequency channels. Moreover, our proposed lattice exhibits the flatband corresponding to a single localized frequency mode inside one unit cell, which is fundamentally different from previous works on other platforms [19]. The eigenstate distributions for other synthetic lattice structures such as those with $\Omega_A:\Omega_B = 4:3$ and $7:5$ hold similar features [39].

The localization position in each spectral unit cell is not fixed when γ is small. In particular, the intensity distributions associated with eigenstates are not localized for small γ, but they gradually become localized when γ becomes

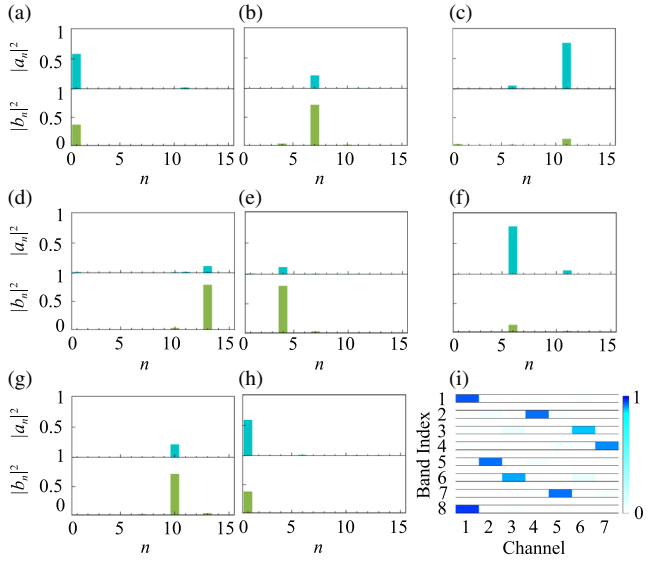

FIG. 3. (a)–(h) The normalized eigenstate distributions of the 8 bands in Fig. 2(e) with $\Omega_A:\Omega_B = 5:3$ and $\gamma = 0.65$ at $k_f = -\pi/(N_A N_B \Omega)$ in the order from top to bottom. The top (bottom) panels represent the normalized eigenstate distributions in ring A (ring B). (i) The eigenstate distribution of the 8 flatbands at 7 frequency channels. Band index refers to bands in Fig. 2(e) in the order from top to bottom.

larger. It is interesting to note that, in 1D synthetic moiré lattice with small unit cell, γ_s is large, and the transition from nonflat to flat band with uniform eigenstate distribution in k_f space as well as the localization of energy on a single mode inside the unit cell are concurrent for larger γ close to the γ_s. On the other hand, in moiré lattice with larger unit cell, the transition from nonflat to flat band occurs when γ is small (because γ_s is smaller). The localization of energy on a single mode presents when one further increases γ [39].

To verify such localization effects, we perform simulations by solving Eqs. (1)–(5) in synthetic moiré lattice with $\Omega_A:\Omega_B = 5:3$ with finite sites $m \in [-44, 60]$, corresponding to 7 unit cells with the center cell having $m = 1, \ldots, 15$. We inject a frequency-comb source field through the waveguide coupled to ring B composed of 15 frequency peaks in the vicinity of modes within $m \in [1, 15]$, with the temporal shape $s = \exp[-3(\Omega t/2\pi - 25)^2/250]$. Detunings $\delta\omega$ between each peak in the input source and each frequency mode are consistent for 15 modes. We set $\delta\omega/\Omega = 0.447,\ 0.162,\ 0.115,\ 0.046,\ -0.046,\ -0.115,\ -0.162,\ -0.447$ to selectively excite 8 bands in Fig. 2(e) with $\gamma = 0.65$, respectively. Signals in both rings are collected via external waveguides for analysis. In Figs. 4(a1)–4(h1), we plot evolutions of intensities for normalized frequency components $I_{A,m,\mathrm{out}}(t)$ and $I_{B,m,\mathrm{out}}(t)$ at the mth mode for different detunings $\delta\omega$, while Figs. 4(a2)–4(h2) show normalized intensities $I_{A,m,\mathrm{out}}$ and $I_{B,m,\mathrm{out}}$ at $t = 50 \cdot 2\pi/\Omega$. One sees only the frequency

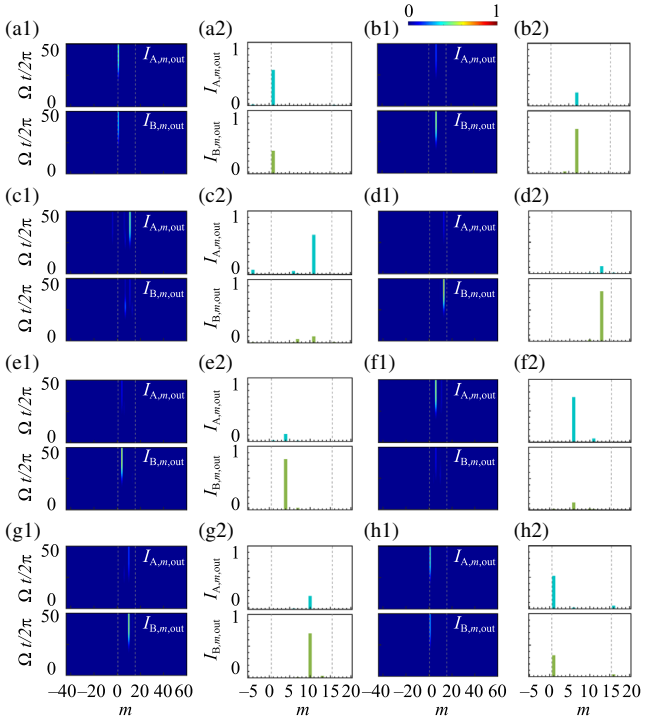

FIG. 4. (a1)–(h1) The evolution of intensities for normalized frequency components $I_{A,m,\mathrm{out}}(t)$ and $I_{B,m,\mathrm{out}}(t)$. (a2)–(h2) The normalized intensities $I_{A,m,\mathrm{out}}$ and $I_{B,m,\mathrm{out}}$ at $t = 50 \cdot 2\pi/\Omega$, for $\delta\omega$ corresponds to 8 bands in Fig. 2(e). The gray dashed lines denote the range of the frequency-comb source.

mode supported by localized modes in Figs. 3(a)–3(h) is excited while others vanish quickly. The excited mode does not evolve into other unit cells either. As comparisons, if we excite the moiré lattice with the same frequency-comb source into rings coupled at the strength $\gamma = 0.1$, whose detunings correspond to the bands in Fig. 2(b), such localization effects disappear [39]. Hence, by taking advantage of the eigenstate characteristic that one flatband is linked to one frequency mode in each unit cell, our results demonstrate the manipulation of spectral localization positions in this 1D synthetic moiré lattice.

In summary, we study an analog model of moiré lattice projected into one-dimensional synthetic frequency dimension, by resonantly coupling two modulated rings at irreducible lengths. When the coupling strength between two rings exceeds the threshold γ_s, all bands are found to become flat and each one along the entire k_f space corresponds to the eigenstate with its energy distribution localized on one frequency mode in one unit cell. We further demonstrate that one can manipulate such localization features by selectively exciting the bands in simulations. Further introduction of photon-photon interactions from optical nonlinearity in the frequency dimension [44] can provide unique opportunities of studying strongly correlated phases [45,46] in 1D synthetic moiré lattice. Our theoretical scheme is potentially valid in future experimental realizations on several optical platforms, such as lithium niobite microrings [47–50], fiber-ring system [26,27,51–54], and on-chip silicon [55–57]. Together, these ingredients provide a flexible platform for generating various moiré lattices using frequency as a synthetic dimension, and also hold potential optical applications such as generating small effective free spectral range by coupling smaller rings in integrated photonics. The controllable localization position inside one adjustable unit cell may inspire more exotic phenomena including the combination of moiré physics with Floquet engineering of topological phases [58].

The research was supported by the National Natural Science Foundation of China (No. 12122407, No. 12192252, No. 11974245, and No. 12104297), National Key Research and Development Program of China (No. 2021YFA1400900). L. Y. thanks the sponsorship from the Yangyang Development Fund and the support from the Program for Professor of Special Appointment (Eastern Scholar) at Shanghai Institutions of Higher Learning. D. L. acknowledges support from the National Research Foundation, Singapore and A*STAR under its CQT Bridging Grant.

*daniel.leykam@gmail.com
†yuanluqi@sjtu.edu.cn

[1] J. M. B. Lopes dos Santos, N. M. R. Peres, and A. H. Castro Neto, Graphene Bilayer with a Twist: Electronic Structure, Phys. Rev. Lett. **99**, 256802 (2007).
[2] R. Bistritzer and A. H. MacDonald, Moiré bands in twisted double-layer graphene, Proc. Natl. Acad. Sci. U.S.A. **108**, 12233 (2011).
[3] I. Brihuega, P. Mallet, H. González-Herrero, G. Trambly de Laissardière, M. M. Ugeda, L. Magaud, J. M. Gómez-Rodríguez, F. Ynduráin, and J. Y. Veuillen, Unraveling the Intrinsic and Robust Nature of van Hove Singularities in Twisted Bilayer Graphene by Scanning Tunneling Microscopy and Theoretical Analysis, Phys. Rev. Lett. **109**, 196802 (2012).
[4] K. Kim, A. DaSilva, S. Huang, B. Fallahazad, S. Larentis, T. Taniguchi, K. Watanabe, B. J. LeRoy, A. H. MacDonald, and E. Tutuc, Tunable moiré bands and strong correlations in small-twist-angle bilayer graphene, Proc. Natl. Acad. Sci. U.S.A. **114**, 3364 (2017).
[5] Q. Tong, H. Yu, Q. Zhu, Y. Wang, X. Xu, and W. Yao, Topological mosaics in moiré superlattices of van der Waals heterobilayers, Nat. Phys. **13**, 356 (2017).
[6] Y. Cao, V. Fatemi, S. Fang, K. Watanabe, T. Taniguchi, E. Kaxiras, and P. Jarillo-Herrero, Unconventional superconductivity in magic-angle graphene superlattices, Nature (London) **556**, 43 (2018).
[7] Y. Cao, V. Fatemi, A. Demir, S. Fang, S. L. Tomarken, J. Y. Luo, J. D. Sanchez-Yamagishi, K. Watanabe, T. Taniguchi, E. Kaxiras, R. C. Ashoori, and P. Jarillo-Herrero, Correlated insulator behaviour at half-filling in magic-angle graphene superlattices, Nature (London) **556**, 80 (2018).

[8] Z. Song, Z. Wang, W. Shi, G. Li, C. Fang, and B. A. Bernevig, All Magic Angles in Twisted Bilayer Graphene are Topological, Phys. Rev. Lett. **123**, 036401 (2019).

[9] K. Tran *et al.*, Evidence for moiré excitons in van der Waals heterostructures, Nature (London) **567**, 71 (2019).

[10] A. Abouelkomsan, Z. Liu, and E. J. Bergholtz, Particle-Hole Duality, Emergent Fermi Liquids, and Fractional Chern Insulators in Moiré Flatbands, Phys. Rev. Lett. **124**, 106803 (2020).

[11] C. Huang, F. Ye, X. Chen, Y. V. Kartashov, V. V. Konotop, and L. Torner, Localization-delocalization wavepacket transition in Pythagorean aperiodic potentials, Sci. Rep. **6**, 32546 (2016).

[12] Q. Fu, P. Wang, C. Huang, Y. V. Kartashov, L. Torner, V. V. Konotop, and F. Ye, Optical soliton formation controlled by angle twisting in photonic moiré lattices, Nat. Photonics **14**, 663 (2020).

[13] P. Wang, Y. Zheng, X. Chen, C. Huang, Y. V. Kartashov, L. Torner, V. V. Konotop, and F. Ye, Localization and delocalization of light in photonic moiré lattices, Nature (London) **577**, 42 (2020).

[14] K. Dong, T. Zhang, J. Li, Q. Wang, F. Yang, Y. Rho, D. Wang, C. P. Grigoropoulos, J. Wu, and J. Yao, Flat Bands in Magic-Angle Bilayer Photonic Crystals at Small Twists, Phys. Rev. Lett. **126**, 223601 (2021).

[15] B. Lou, N. Zhao, M. Minkov, C. Guo, M. Orenstein, and S. Fan, Theory for Twisted Bilayer Photonic Crystal Slabs, Phys. Rev. Lett. **126**, 136101 (2021).

[16] H. Tang, X. Ni, F. Du, and E. Mazur, On-chip light trapping in bilayer moiré photonic crystal slabs, Appl. Phys. Lett. **121**, 231702 (2022).

[17] D. Vu and S. Das Sarma, Moiré versus Mott: Incommensuration and Interaction in One-Dimensional Bichromatic Lattices, Phys. Rev. Lett. **126**, 036803 (2021).

[18] W. Wang, W. Gao, X. Chen, F. Shi, G. Li, J. Dong, Y. Xiang, and S. Zhang, Moiré Fringe Induced Gauge Field in Photonics, Phys. Rev. Lett. **125**, 203901 (2020).

[19] D. X. Nguyen, X. Letartre, E. Drouard, P. Viktorovitch, H. C. Nguyen, and H. S. Nguyen, Magic configurations in moiré superlattice of bilayer photonic crystals: Almost-perfect flatbands and unconventional localization, Phys. Rev. Res. **4**, L032031 (2021).

[20] T. H. Talukdar, A. L. Hardison, and J. D. Ryckman, Moiré effects in silicon photonic nanowires, ACS Photonics **9**, 1286 (2022).

[21] L. Yuan, Q. Lin, M. Xiao, and S. Fan, Synthetic dimension in photonics, Optica **5**, 1396 (2018).

[22] T. Ozawa and H. M. Price, Topological quantum matter in synthetic dimensions, Nat. Rev. Phys. **1**, 349 (2019).

[23] E. Lustig and M. Segev, Topological photonics in synthetic dimensions, Adv. Opt. Photonics **13**, 426 (2021).

[24] L. Yuan, M. Xiao, Q. Lin, and S. Fan, Synthetic space with arbitrary dimensions in a few rings undergoing dynamic modulation, Phys. Rev. B **97**, 104105 (2018).

[25] D. Yu, B. Peng, X. Chen, X.-J. Liu, and L. Yuan, Topological holographic quench dynamics in a synthetic frequency dimension, Light Sci. Appl. **10**, 209 (2021).

[26] K. Wang, A. Dutt, C. C. Wojcik, and S. Fan, Topological complex-energy braiding of non-Hermitian bands, Nature (London) **598**, 59 (2021).

[27] G. Li, L. Wang, R. Ye, S. Liu, Y. Zheng, L. Yuan, and X. Chen, Observation of flat-band and band transition in the synthetic space, Adv. Opt. Photonics **4**, 036002 (2022).

[28] L. Yuan, A. Dutt, and S. Fan, Synthetic frequency dimensions in dynamically modulated ring resonators, APL Photonics **6**, 071102 (2021).

[29] Q. Lin, M. Xiao, L. Yuan, and S. Fan, Photonic Weyl point in a two-dimensional resonator lattice with a synthetic frequency dimension, Nat. Commun. **7**, 13731 (2016).

[30] Z.-D. Song and B. A. Bernevig, Magic-Angle Twisted Bilayer Graphene as a Topological Heavy Fermion Problem, Phys. Rev. Lett. **129**, 047601 (2022).

[31] D. Yu, L. Yuan, and X. Chen, Isolated photonic flatband with the effective magnetic flux in a synthetic space including the frequency dimension, Laser Photonics Rev. **14**, 2000041 (2020).

[32] K. Oda, N. Takato, T. Kominato, and H. Toba, Channel selection and stabilization technique for a waveguide-type 16-channel frequency selection switch for optical FDM distribution systems, IEEE Photonics Technol. Lett. **1**, 137 (1989).

[33] S. Etemad, P. Toliver, R. Menendez, J. Young, T. Banwell, S. Galli, J. Jackel, P. Delfyett, C. Price, and T. Turpin, Spectrally efficient optical CDMA using coherent phase-frequency coding, IEEE Photonics Technol. Lett. **17**, 929 (2005).

[34] Y. E. Kraus, Y. Lahini, Z. Ringel, M. Verbin, and O. Zilberberg, Topological States and Adiabatic Pumping in Quasicrystals, Phys. Rev. Lett. **109**, 106402 (2012).

[35] M. Verbin, O. Zilberberg, Y. E. Kraus, Y. Lahini, and Y. Silberberg, Observation of Topological Phase Transitions in Photonic Quasicrystals, Phys. Rev. Lett. **110**, 076403 (2013).

[36] Z. V. Vardeny, A. Nahata, and A. Agrawal, Optics of photonic quasicrystals, Nat. Photonics **7**, 177 (2013).

[37] S. Longhi, Topological Phase Transition in non-Hermitian Quasicrystals, Phys. Rev. Lett. **122**, 237601 (2019).

[38] O. Zilberberg, Topology in quasicrystals, Opt. Mater. Express **11**, 1143 (2021).

[39] See Supplemental Material at http://link.aps.org/supplemental/10.1103/PhysRevLett.130.143801 for equations to describe the scattering process, description of the criterion for γ_s, effective models in the two limits, the relationship between band index and localization position in the eigenstate distribution, eigenstate distributions of lattice structures $\Omega_A:\Omega_B = 4:3$ and $\Omega_A:\Omega_B = 7:5$, eigenstate distributions versus γ, and simulations for $\Omega_A:\Omega_B = 5:3$ at $\gamma = 0.1$, which includes Refs. [40,41].

[40] E. Tang, J.-W. Mei, and X.-G. Wen, High-Temperature Fractional Quantum Hall States, Phys. Rev. Lett. **106**, 236802 (2011).

[41] E. J. Bergholtz and Z. Liu, Topological flat band models and fractional Chern insulators, Int. J. Mod. Phys. B **27**, 1330017 (2013).

[42] B. E. A. Saleh and M. C. Teich, Fundamentals of photonics, *Wiley Series in Pure and Applied Optics* (Wiley-Interscience, Hoboken, NJ, 2007).

[43] S. Fan, W. Suh, and J. D. Joannopoulos, Temporal coupled-mode theory for the Fano resonance in optical resonators, J. Opt. Soc. Am. A **20**, 569 (2003).

[44] L. Yuan, A. Dutt, M. Qin, S. Fan, and X. Chen, Creating locally interacting Hamiltonians in the synthetic frequency dimension for photons, Photonics Res. **8**, B8 (2020).
[45] K. P. Nuckolls, M. Oh, D. Wong, B. Lian, K. Watanabe, T. Taniguchi, B. A. Bernevig, and A. Yazdani, Strongly correlated Chern insulators in magic-angle twisted bilayer graphene, Nature (London) **588**, 610 (2020).
[46] C. Shen, P. J. Ledwith, K. Watanabe, T. Taniguchi, E. Khalaf, A. Vishwanath, and D. K. Efetov, Dirac spectroscopy of strongly correlated phases in twisted trilayer graphene, Nat. Mater. **22**, 316 (2023).
[47] M. Zhang, C. Wang, R. Cheng, A. Shams-Ansari, and M. Lončar, Monolithic ultra-high-Q lithium niobate microring resonator, Optica **4**, 1536 (2017).
[48] C. Wang, M. Zhang, B. Stern, M. Lipson, and M. Lončar, Nanophotonic lithium niobate electro-optic modulators, Opt. Express **26**, 1547 (2018).
[49] M. Zhang, C. Wang, Y. Hu, A. Shams-Ansari, T. Ren, S. Fan, and M. Lončar, Electronically programmable photonic molecule, Nat. Photonics **13**, 36 (2019).
[50] Y. Hu, C. Reimer, A. Shams-Ansari, M. Zhang, and M. Loncar, Realization of high-dimensional frequency crystals in electro-optic microcombs, Optica **7**, 1189 (2020).
[51] G. Li, Y. Zheng, A. Dutt, D. Yu, Q. Shan, S. Liu, L. Yuan, S. Fan, and X. Chen, Dynamic band structure measurement in the synthetic space, Sci. Adv. **7**, eabe4335 (2021).
[52] A. Dutt, Q. Lin, L. Yuan, M. Minkov, M. Xiao, and S. Fan, A single photonic cavity with two independent physical synthetic dimensions, Science **367**, 59 (2020).
[53] K. Wang, A. Dutt, K. Y. Yang, C. C. Wojcik, J. Vučković, and S. Fan, Generating arbitrary topological windings of a non-Hermitian band, Science **371**, 1240 (2021).
[54] H. Chen, N. Yang, C. Qin, W. Li, B. Wang, T. Han, C. Zhang, W. Liu, K. Wang, H. Long, X. Zhang, and P. Lu, Real-time observation of frequency Bloch oscillations with fibre loop modulation, Light Sci. Appl. **10**, 48 (2021).
[55] Q. Xu, D. Fattal, and R. G. Beausoleil, Silicon microring resonators with 1.5-μm radius, Opt. Express **16**, 4309 (2008).
[56] L. D. Tzuang, M. Soltani, Y. H. D. Lee, and M. Lipson, High RF carrier frequency modulation in silicon resonators by coupling adjacent free-spectral-range modes, Opt. Lett. **39**, 1799 (2014).
[57] A. Balčytis, T. Ozawa, Y. Ota, S. Iwamoto, J. Maeda, and T. Baba, Synthetic dimension band structures on a Si CMOS photonic platform, Sci. Adv. **8**, eabk0468 (2022).
[58] I. Martin, G. Refael, and B. Halperin, Topological Frequency Conversion in Strongly Driven Quantum Systems, Phys. Rev. X **7**, 041008 (2017).